

A multi-epoch spectroscopic study of the BAL quasar APM 08279+5255

II. Emission- and absorption-line variability time lags

F. G. Saturni^{1,2}, D. Trevese¹, F. Vagnetti³, M. Perna⁴, and M. Dadina⁵

¹ Università degli Studi di Roma “La Sapienza”, p.le A. Moro 5, I-00185 Rome (Italy)
e-mail: saturnfg@roma1.infn.it

² Università degli Studi “Roma Tre”, via della Vasca Navale 84, I-00146 Rome (Italy)

³ Università di Roma “Tor Vergata”, via della Ricerca Scientifica 1, I-00133 Rome (Italy)

⁴ Università di Bologna, via Zamboni 33, I-40126 Bologna (Italy)

⁵ INAF-IASF Bologna, via Gobetti 101, I-40129 Bologna (Italy)

Received 2015 August 10; accepted 2015 December 4

ABSTRACT

Context. The study of high-redshift bright quasars is crucial to gather information about the history of galaxy assembly and evolution. Variability analyses can provide useful data on the physics of the quasar processes and their relation with the host galaxy.

Aims. In this study, we aim at measuring the black hole mass of the bright lensed BAL QSO APM 08279+5255 at $z = 3.911$ through reverberation mapping, and at updating and extending the monitoring of its C IV absorption line variability.

Methods. Thanks to 138 *R*-band photometric data and 30 spectra available over 16 years of observations, we perform the first reverberation mapping of the Si IV and C IV emission lines for a high-luminosity quasar at high redshift. We also cross-correlate the C IV absorption equivalent width variations with the continuum light curve, in order to estimate the recombination time lags of the various absorbers and infer the physical conditions of the ionised gas.

Results. We find a reverberation-mapping time lag of ~ 900 rest-frame days for both Si IV and C IV emission lines. This is consistent with an extension of the BLR size-to-luminosity relation for active galactic nuclei up to a luminosity of $\sim 10^{48}$ erg s⁻¹, and implies a black hole mass of $10^{10} M_{\odot}$. Additionally, we measure a recombination time lag of ~ 160 days in the rest frame for the C IV narrow absorption system, which implies an electron density of the absorbing gas of $\sim 2.5 \cdot 10^4$ cm⁻³.

Conclusions. The measured black hole mass of APM 08279+5255 indicates that the quasar resides in an under-massive host-galaxy bulge with $M_{\text{bulge}} \sim 7.5 M_{\text{BH}}$, and that the lens magnification is lower than ~ 8 . Finally, the inferred electron density of the narrow-line absorber implies a distance of the order of 10 kpc of the absorbing gas from the quasar, placing it within the host galaxy.

Key words. galaxies: active – quasars: general – quasars: absorption lines – quasars: emission lines – quasars: supermassive black holes – quasars: individual: APM 08279+5255

1. Introduction

Quasars are broad-line, high-luminosity active galactic nuclei (AGNs) with spectral features surprisingly similar to those of the Seyfert galaxies, despite a difference in luminosity of several orders of magnitude. This implies a common process at the base of their existence. Moreover, quasars distinguish themselves for emitting at all wavelengths from radio to gamma rays, with a total energy emission comparable to that of a bright galaxy. The commonly accepted model able to match the observations is the accretion of gas around a supermassive black hole (SMBH; Salpeter 1964; Zel’dovich & Novikov 1965).

The similarity in quasar spectra naturally leads to build a unified scenario for the structure of quasars (see e.g. Urry & Padovani 1995 for a review). In the simplest one, ionised gas clouds orbit around the black hole at radii larger than the accretion disk responsible of the continuum emission, producing the broad (from a broad-line region, BLR, still relatively close to the central black hole) and narrow (from a farther narrow-line region, NLR) emission lines. At intermediate orientations between the accretion disk plane and its axis, high-velocity winds can be launched under the action of the radiation pressure, thus originating the broad-absorption line (BAL) phenomenon when

the quasar is viewed along the wind (Weymann & Foltz 1983; Turnshek 1988; Elvis 2000).

Assuming that such features are common to all quasars, the only two parameters which the quasar structure depends on are the SMBH mass and the quasar inclination angle with respect to the line of sight. The first quantity has great relevance in cosmological studies: in fact, SMBHs trace large-scale structures and co-evolve with their host galaxies (see e.g. Cattaneo et al. 2009 and refs. therein), thus giving information about the quantity of matter in the Universe and the history of galaxy assembly.

Currently, the only direct way to estimate the SMBH mass beyond the local Universe is through reverberation mapping (RM; Gaskell & Peterson 1987; Edelson & Krolik 1988; White & Peterson 1994; Peterson 1997), by which the time lag t_{lag} between the quasar broad emission-line and continuum variability, hence the size of the BLR $R_{\text{BLR}} = ct_{\text{lag}}$, can be measured. Under the hypothesis of virialised orbits in the BLR, the black hole mass M_{BH} is given by:

$$M_{\text{BH}} = f \frac{ct_{\text{lag}} \Delta v^2}{G} \quad (1)$$

Here, the form factor f summarises all the ignorance about the shape and inclination with respect to the line of sight of the

BLR, that can significantly alter the final value of M_{BH} , while Δv is the full width at half maximum (FWHM) of the considered emission line. Under reasonable assumptions on the distribution of gas clouds in the BLR (i.e., assuming some physical value for f), this formula gives a measurement of M_{BH} in principle for all classes of active galactic nuclei (AGNs) with broad emission lines. In this way, relations between mass, line width and quasar luminosity (e.g., McLure & Dunlop 2004; Vestergaard & Peterson 2006; Shen et al. 2011) can be computed, and the SMBH mass can be estimated from single-epoch quasar spectra. This avoids the necessity of a RM for each object, allowing to obtain mass estimates for a large number of sources.

The application of the RM method was initially limited to low-luminosity, local AGNs like the Seyfert galaxies, that have variability time scales from days to weeks at most (Wandel et al. 1999; Peterson et al. 2004). Subsequently, it was applied to low-redshift quasars ($z < 0.4$; Kaspi et al. 2000). For higher-luminosity, higher-redshift quasars, the increase of the BLR size with luminosity and the cosmological time dilation increase the variability time scales up to years, thus making campaigns for quasar RM observationally expensive. Until now, only three luminous, high-redshift quasars have RM mass measurements (Kaspi et al. 2007; Chelouche et al. 2012; Trevese et al. 2014); this lack of information at high masses and luminosities means that the application of single-epoch mass-luminosity relations to quasars is actually an extrapolation based on data from AGNs of moderate redshift only, making subject to possible biases the current black hole mass estimates of quasars in cosmological surveys (e.g., Shen et al. 2011).

Broad absorption-line quasars (BAL QSOs; Lynds 1967; Weymann & Foltz 1983; Turnshek 1988; Elvis 2000) are a very important test for unified scenarios, since the mechanisms to launch a highly ionised, high-velocity (up to $\sim 0.2c$) absorbing outflow are still poorly known. The exact location, structure and physical properties of BAL outflows are difficult to introduce in unification schemes for quasars.

BAL variability (e.g., Barlow et al. 1992; Gibson et al. 2008; Capellupo et al. 2011; Trevese et al. 2013) is one of the main ways to gather information about the gas producing the broad absorption features, such as physical (density, temperature, ionisation) and geometrical (location, opening angle, bending) properties of the outflow. Several programmes to study BAL variability are going on, based either on single objects with multi-year observations (Barlow et al. 1992; Krongold et al. 2010; Hall et al. 2011; Trevese et al. 2013; Grier et al. 2015) or on *ensemble* analyses of quasar samples with a few (up to 10) observations per object (Barlow 1993; Lundgren et al. 2007; Gibson et al. 2008; Capellupo et al. 2011, 2012, 2013; Filiz Ak et al. 2013). Currently, the possible explanation of the BAL variability over multi-year time scales consider changes either in the gas ionisation level or in the covering factor, although the second possibility is favoured since: (i) the variations tend to occur in narrow portions of BAL troughs (e.g., Filiz Ak et al. 2013), and (ii) they generally do not correlate with changes in the observed continuum (Gibson et al. 2008; Capellupo et al. 2011; but see Trevese et al. 2013).

In this study, we take advantage of our long-term monitoring programme of high-luminosity quasars (Trevese et al. 2007) to increase the data statistics about the bright BAL QSO APM 08279+5255, in order to update our study on its C IV absorption variability (Trevese et al. 2013, Paper I henceforth; Saturni et al. 2014) and to obtain estimates of its black hole mass through RM of Si IV and C IV emission lines. APM 08279+5255 is one of the most luminous quasars, discovered in 1998 by Irwin et al.

(1998). It is well known for its gravitational lensing, first confirmed case of a lens with odd number of image components (Lewis et al. 2002). Additionally, its redshift inferred from the high-ionisation emission lines (N V, Si IV, C IV and C III) is $z = 3.87$ (Irwin et al. 1998), which corresponds to an outflow velocity of $\sim 2500 \text{ km s}^{-1}$ with respect to the systemic redshift $z = 3.911$ derived from the CO emission lines (Downes et al. 1999).

The paper is organised as follows: in Sect. 2, we briefly present the target of the observations and describe the adopted observational strategy and data reduction; in Sect. 3, we present the line-to-continuum RM time lags; in Sect. 4, we update the absorption variability study of APM 08279+5255 with new data; finally, in Sect. 5 we discuss APM 08279+5255 black hole mass estimates and absorption variability, summarising all the findings in Sect. 6. Throughout this paper, we use the terms “quasar” and “QSO” interchangeably, and adopt a concordance cosmology with $H_0 = 70 \text{ km s}^{-1} \text{ Mpc}^{-1}$, $\Omega_M = 0.3$ and $\Omega_\Lambda = 0.7$.

2. Observations and data reduction

2.1. The reverberation mapping campaign

Our RM campaign of luminous quasars started in 2003 at the Asiago Observatory, Italy (Trevese et al. 2007). Motivated by the work of Netzer (2003) about the possible biases introduced in galaxy mass estimates by an overestimation of their black hole mass M_{BH} , the goal was to measure M_{BH} of some intrinsically bright objects in order to extend the BLR size-luminosity relationships for AGNs (Peterson et al. 2005; Kaspi et al. 2007) to luminosities greater than $\sim 10^{46} \text{ erg s}^{-1}$. Both *R*-band photometric data and spectra have been obtained with the Asiago Faint Object Spectrograph and Camera (AFOSC) at the 1.82 m Copernico telescope (Asiago, Italy). Since December 2012, the campaign is going on at the 1.52 m Cassini telescope (Loiano, Italy), with the Bologna Faint Object Spectrograph and Camera (BFOSC).

The procedure of observation and data reduction is explained in detail in previous papers (Trevese et al. 2007, 2013, 2014). Here we simply recall that the instrument was set in order to simultaneously observe the quasar and a star *S* of comparable magnitude ($R = 14.66$; Röser et al. 2010), located at $\alpha 08 31 22.3 \delta +52 44 58.6$ (J2000), which has been adopted as calibration reference for both photometry and spectra. The QSO and the star are observed in the same slit. A wide slit of 8" (on AFOSC) or 12" (on BFOSC) was adopted to avoid light losses due to small misalignments or differential refraction, that would produce artificial variability. In this way, we obtain differential magnitudes ΔR between the quasar and the reference star from the photometry, and spectral ratios Q/S between the uncalibrated quasar (*Q*) and stellar (*S*) spectra. The latter are then multiplied to a stellar spectrum of *S* taken at MJD = 55,894.5 and calibrated through standard IRAF techniques: assuming that the reference star is non-variable, this provides a flux calibration preserving the quasar variability. An example of these spectra is shown in Fig. 1. In total, we have collected 28 *R*-band photometric data and 30 spectra until March 2015, part of which has been already analysed in previous papers focussed on the C IV absorption variability (Paper I; Saturni et al. 2014).

The RM technique requires to construct a quasar continuum light curve (LC) and an emission-line LC for each line considered. Therefore, we have converted our magnitude differences ΔR between quasar and reference star to flux ratios F_Q/F_S ; since we compute an emission-line contribution to the total *R*-band

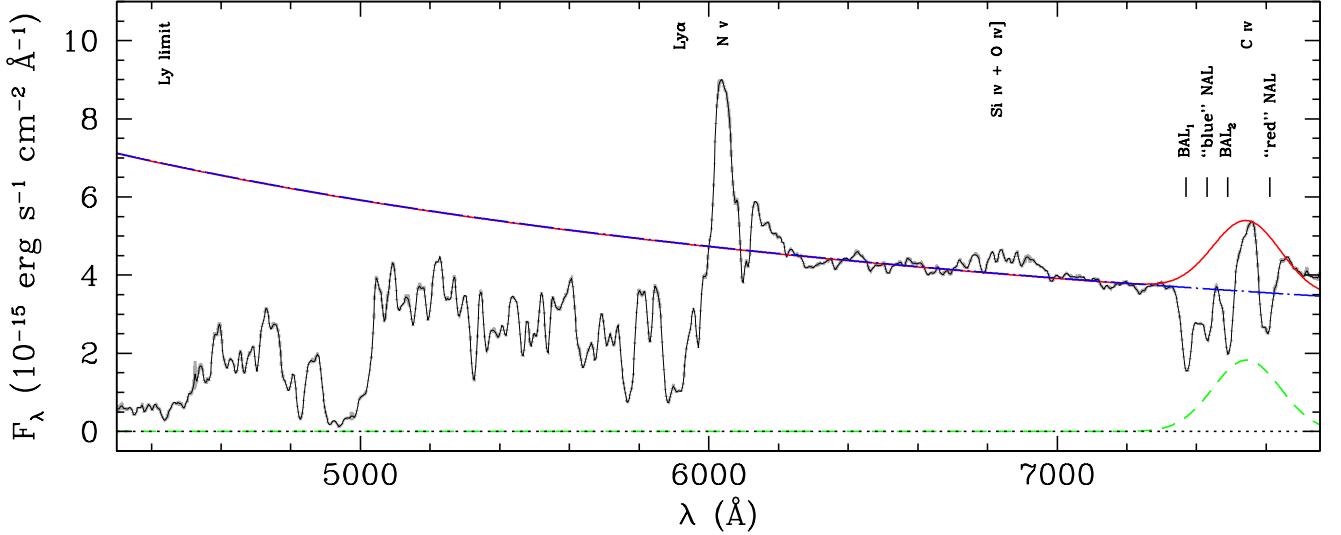


Fig. 1. The de-reddened spectrum of APM 08279+5255 taken at MJD = 52,695 at the 1.82 m Copernico telescope (Asiago, Italy). Superimposed to the spectrum (*black solid line*), a power-law continuum (*blue dot-dashed line*), a Gaussian fit of the C IV emission line (*green dashed line*) and the combination of these two components into a single pseudo-continuum (*red solid line*) are shown. The dotted line marks the flux zero level. The major absorption features are marked with the identifiers used in the text (see Sect. 4) and ticks. The positions of the Lyman limit at $\lambda 912$ Å in the rest frame and of the major emission lines are also indicated.

flux of $\sim 11\%$ only, we assume that our photometry is well tracing the quasar UV rest-frame continuum variability, and adopt it as the reference to construct APM 08279+5255 continuum LC. We have then computed the quasar continuum flux from our series of spectra in a rest-frame spectral interval of 100 Å around $\lambda = 1350$ Å. The LC obtained in this way differs from the *R*-band photometry by only a scale factor; this, assumed constant for all spectra, has been computed over a time interval in which the quasar flux level remains approximately constant, and has been verified to provide a good match to the *R*-band photometry also in the presence of flux variations. Therefore, we have scaled by this factor the spectral continuum LC to the photometric data, and have added it to the full data set of the continuum LC. This improves our statistics to 58 points tracing the continuum variations of APM 08279+5255. In Tab. 2, we report our spectro-photometric data together with the data collected from the literature described in the next subsection.

2.2. Data from the literature

As in Paper I, we have added the photometric data of Lewis et al. (1999) to our data set, after re-scaling their measurements from their reference star S_1 , which is always serendipitously included in our field of view, to our reference star S . This provides us with additional 23 photometric points. One last data set of 59 *V*-band points, scaled to our *R*-band photometry in the same way of our spectral continuum fluxes, came from the Catalina Sky Survey (Drake et al. 2009). In this way, we end up with a total of 138 continuum data points for APM 08279+5255, that along with 30 spectra constitute so far the largest data set collected for a quasar at such high redshift. Tab. 2 summarises our observations and the literature data: we give the observation date MJD $-50,000$ in Col. 1, the telescope in Col. 2, the observation type (spectroscopic or photometric) in Col. 3, the continuum flux ratios F_Q/F_S referred to the *R*-band fluxes (as explained in the

previous subsection) in Col. 4, the Si IV and C IV emission-line fluxes in Col. 5 and 6 respectively (see Sect. 3).

We also take advantage of the existence of further five spectra of APM 08279+5255 available in the literature (Irwin et al. 1998; Ellison et al. 1999; Hines et al. 1999; Lewis et al. 2002; Saturni et al. 2015, in prep.), introducing them into our monitoring as well. Unfortunately, due to the lack of a uniform flux calibration these spectra cannot be used in our RM, and hence will be added to the current data set only for the purposes of updating the C IV absorption variability study presented in Paper I and Saturni et al. (2014), which requires only fluxes normalised to the local continuum. Only the HST/STIS spectrum from Lewis et al. (2002) has been used in the RM, but for the sole purpose of determining the C IV emission line width to be used in the RM measurement of APM 08279+5255 SMBH mass; this is motivated by the fact that this spectrum is taken outside the atmosphere, thus avoiding the telluric absorption by the Fraunhofer A band on the residual C IV emission-line wing.

3. Reverberation mapping of the Si IV and C IV emission lines

Thanks to our long-time monitoring, we are now able to perform the RM of APM 08279+5255. This is done by cross-correlating the variability of the *R*-band flux tracing the continuum with the Si IV and C IV emission-line fluxes, in order to find the most probable lag between continuum and line variations. The LCs to be used in this process, shown in Fig. 2, are constructed as follows:

- APM 08279+5255 spectrum is reddened by a foreground absorber at $z \sim 1$ (likely the so-far invisible lensing galaxy; Ellison et al. 2004), with a *V*-band reddening parameter $A_V \sim 0.5$ mag (Petitjean et al. 2000): in order to obtain a better power-law fit to the continuum, we de-redden our series of spectra with a Small-Magellanic-Cloud-like extinction (Pei 1992) produced at $z = 1.062$ (Ellison et al. 2004).

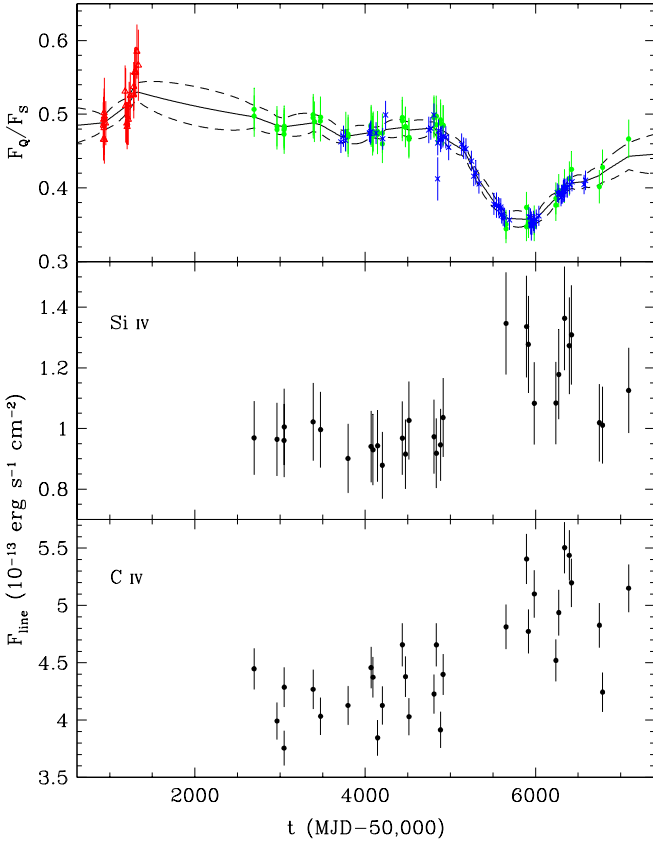


Fig. 2. Upper panel: *R*-band continuum light curve of APM 08279+5255. The (Lewis et al. 1999) photometric campaign (red triangles), the Asiago and Loiano (Trevese et al. 2007, 2013, 2014) RM campaign (green dots) and the rescaled V-band Catalina photometry (blue crosses) are all included. Superimposed to the data, the best-fit DRW variability model computed by JAVELIN (Zu et al. 2011) is shown (black solid line) delimited by its error boundaries at 68% probability (black dashed lines). Middle panel: Si IV light curve. Lower panel: C IV light curve.

This function is fixed at all epochs, hence it does not introduce any noise in the variability;

- for all the spectra, we evaluate the Si IV flux by subtracting a power-law continuum computed at each epoch over two wavelength intervals, $\lambda\lambda 6620 - 6680$ and $\lambda\lambda 7000 - 7100$ in the observer frame, adjacent to that emission line and free of other emission or absorption features. The Si IV flux is then defined as the integral of the line flux in the interval $\lambda\lambda 6680 - 7000$;
- finally, we apply the same fitting procedure described in Paper I and Saturni et al. (2014) to the C IV emission line, assumed Gaussian, and compute its line flux as the integral of the resulting fitting function at each epoch. In this procedure, only the line amplitude is allowed to vary, whereas the peak position is fixed to the C IV $\lambda 1549$ at $z = 3.87$, and the Gaussian width is fixed to the value $\sigma_g = 3200 \text{ km s}^{-1}$ obtained through a fit performed onto the HST/STIS high-resolution spectrum (Lewis et al. 2002), which is free of the O_2 telluric absorption on the C IV red wing.

We report all the emission-line fluxes in the fifth and sixth columns of Tab. 2 together with their 1σ errors.

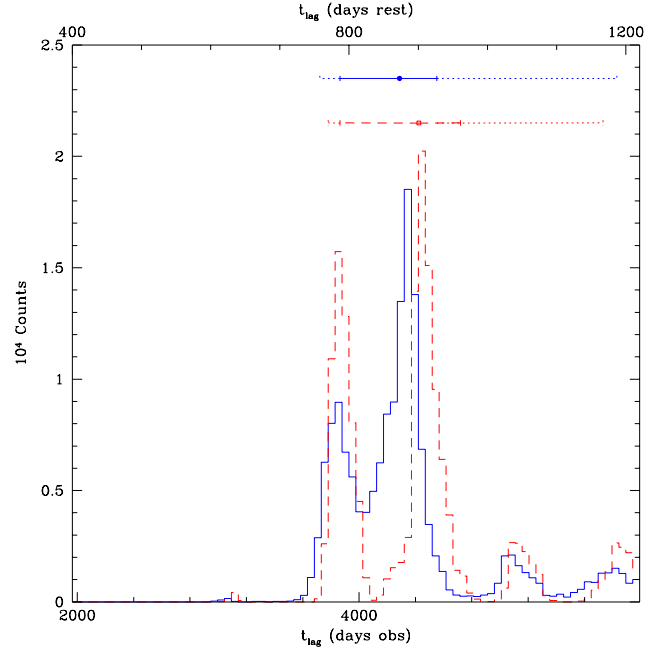


Fig. 3. Posterior distributions of the Si IV (blue solid histogram) and C IV (red dashed histogram) RM time lags computed with JAVELIN. The time-lag mean values (blue point and red square) for each distribution are shown, together with their corresponding confidence intervals at 68% (colour and line-type codes as per the histograms) and at 95% probability (dotted error bars).

In order to determine the emission-line time lag, we recall that the usual method consists in evaluating the peak or centroid of the line-to-continuum cross-correlation function (CCF). This can be constructed either by computing a discrete correlation function (DCF; Edelson & Krolik 1988) or via an interpolation of the LCs (ICCF; Gaskell & Peterson 1987; White & Peterson 1994). However, CCFs provide consistent results only for well-sampled LCs, instead presenting technical problems in the case of poor sampling (Peterson 1993; Welsh 1999). In particular, the DCF sensitivity to real correlation decreases. An estimate of the confidence interval on the measured time lag can be obtained through the DCF z -transformation method (ZDCF) by Alexander (1997, 2013); however, this requires to eliminate from each DCF bin all points corresponding to pairs of epochs with measured data in common. Thus, this is hardly applicable in our case, where the sampling is particularly poor.

We therefore evaluate the RM time lags of SI IV and C IV with the JAVELIN code¹, based on its previous version SPEAR (Stochastic Process Estimation for AGN Reverberation) by Zu et al. (2011). With respect to traditional CCFs, the advantage of this method, whose statistical bases date back to Press et al. (1992); Rybicki & Press (1992) with a first application in Rybicki & Kleyana (1994), is that it makes use of an interpolation algorithm in which the entire data set contributes to each interpolated point, under the assumption that the emission-line LCs $F_l(t)$ are a scaled, smoothed and delayed version of the continuum LC $F_c(t)$. The QSO continuum LC is then modeled with a damped random walk (DRW) process described by a damping time scale τ_d and an rms variability amplitude σ (Kelly

¹ Available at <http://www.astronomy.ohio-state.edu/~yingzu/codes.html>.

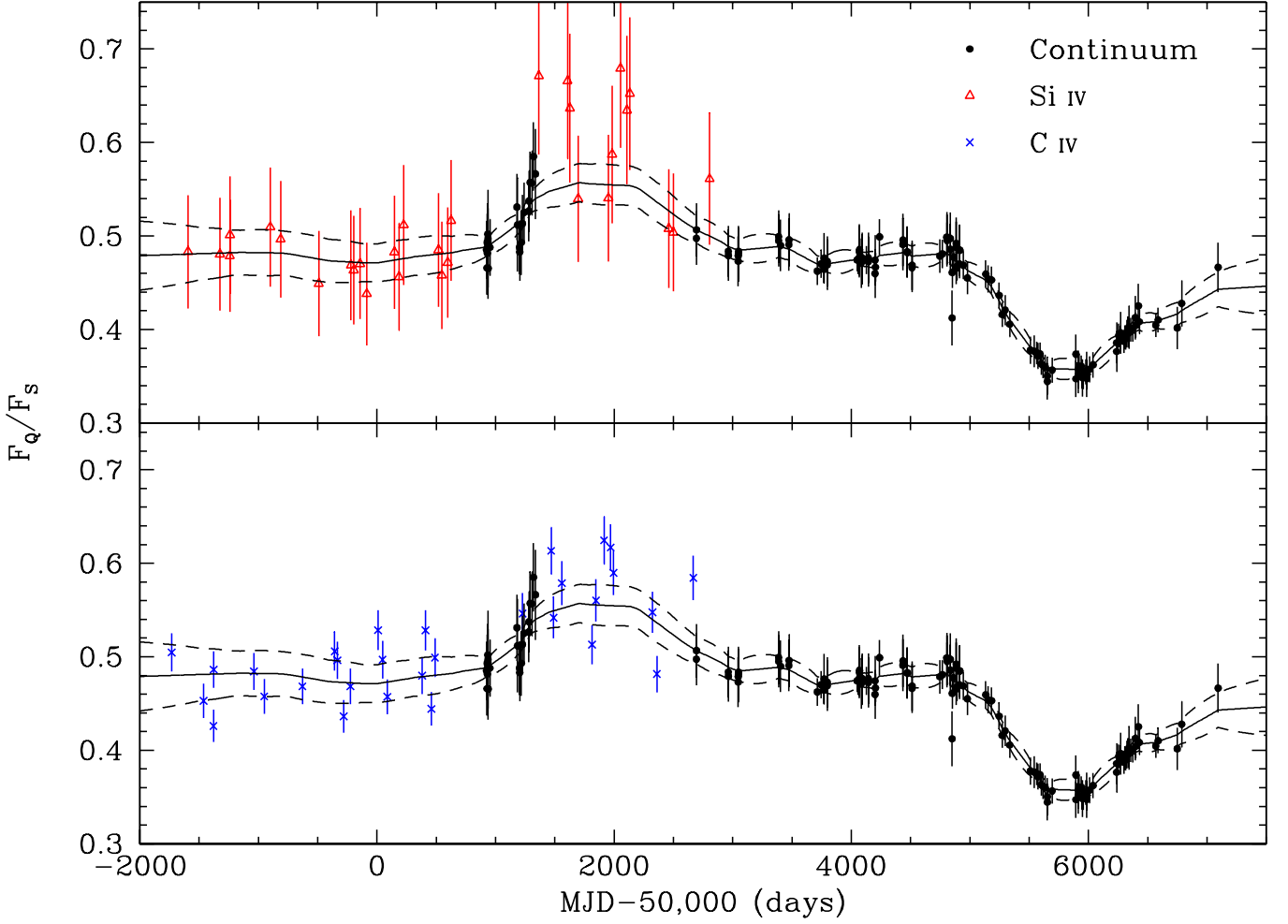


Fig. 4. APM 08279+5255 light curve composed with the continuum (*black dots*) and emission line fluxes, the latter scaled in intensity and shifted in time of their JAVELIN lags of 837 and 901 rest-frame days respectively to mimic the original continuum light curve that is reverberated by the quasar BLR. *Upper panel:* continuum and Si IV (*red triangles*). *Lower panel:* continuum and C IV (*blue crosses*). In both panels, a DRW continuum, fitted by JAVELIN to the data with the damping time scale τ_d blocked to that of the continuum fit, is shown superimposed to the light curve (*solid line*) along with its 1σ error band (*dashed lines*).

et al. 2009; Kozłowski et al. 2010; MacLeod et al. 2010; Zu et al. 2013). This is realised through the application of statistical weights that are determined from the auto-correlation functions of the data.

The emission-line LC is obtained from the continuum LC through the convolution with a transfer function $\Psi(t)$:

$$F_l(t) = \int \Psi(t') F_c(t - t') dt' \quad (2)$$

In this analysis, we adopt for $\Psi(t)$ the simple analytic top-hat form as done by Zu et al. (2011), of width Δ and area A :

$$\Psi(t) = \frac{A}{\Delta}, \quad |t - t_{lag}| \leq \Delta, \text{ and zero elsewhere.} \quad (3)$$

This choice is based on the fact that the resulting emission-line lag t_{lag} does not depend strongly on the specific form of $\Psi(t)$ (Rybicki & Kleya 1994). A maximum-likelihood code provides the five best-fit parameters (τ_d , σ , t_{lag} , A and Δ) for the DRW model that describes the continuum LC and the top-hat transfer function. Finally, confidence limits on the fit parameters are obtained through Monte-Carlo Markov chain (MCMC) iterations.

With respect to traditional CCFs, the model-dependent nature of JAVELIN has the advantage of producing smaller lag uncertainties (Zu et al. 2011).

In order to verify that the result of JAVELIN does not depend on the assumed model, we compute the classical ICCF and DCF via its z -transformation (ZDCF) for each pair of line and continuum LCs, and evaluate the corresponding RM time lags with their uncertainties. Although in our case the CCFs have low statistical significance, they are completely model-independent.

The uncertainty on the ICCF lag is estimated by applying the “flux randomisation and random sample selection” method (FR/RSS) by Peterson et al. (1998). This method allows to compute the statistical distribution of the line-to-continuum time lags by iterating the ICCF procedure over undersampled continuum and emission-line LCs, altering the remaining data by adding a random noise with a Gaussian distribution whose standard deviation is the 1σ error on each measured point. In order to compute the ZDCF time lag and the uncertainty on the peak position, we use the routines made available online by T. Alexander².

² Both scripts are available at <http://wwo.weizmann.ac.il/weizsites/tal/research/software/>.

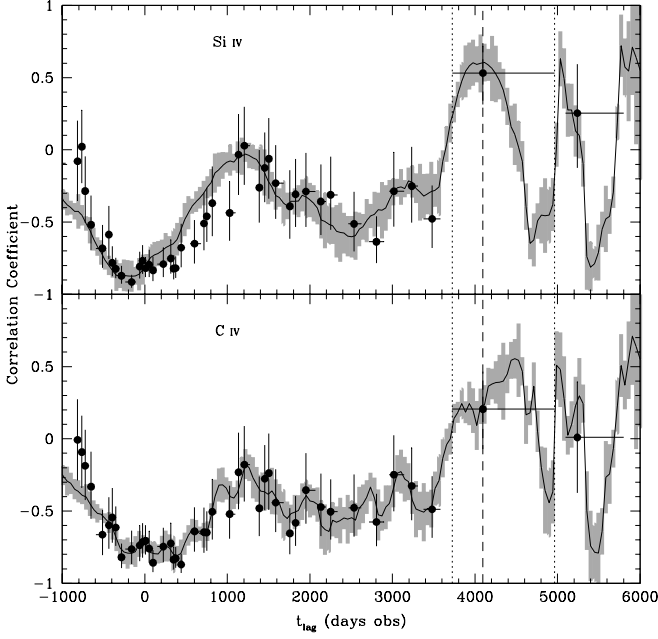


Fig. 5. Upper panel: ICCF (solid line) with its 1σ error (grey area) and ZDCF (black points) for the continuum and the Si IV emission line. Lower panel: same as in the upper panel, but for the continuum and the C IV emission line. The ZDCF is computed over 15 uncorrelated points per bin, and finds a simultaneous peak for the two emission features at $t_{\text{lag}} = 4095^{+867}_{-369}$ days in the observer frame that is marked in the plot (dashed line and dotted lines).

In Sect. 3.1 and 3.2, we respectively report the RM time lags found with the analysis done by JAVELIN, and those found through the CCFs for comparison.

3.1. Reverberation mapping with JAVELIN

As a first step, we apply the JAVELIN method to study the correlation of the individual Si IV and C IV lines with the continuum. Due to our unprecedented long-time monitoring, we are able to probe time lags in the observer frame up to ~ 6000 days, corresponding to ~ 1200 rest-frame days at $z = 3.911$. The analysis with JAVELIN gives $t_{\text{lag}}^{\text{JAV}}(\text{Si IV}) = 4180^{+1035}_{-323}$ days in the observer frame and $t_{\text{lag}}^{\text{JAV}}(\text{C IV}) = 4243^{+337}_{-355}$ days, thus suggesting that the BLR emitting the Si IV and the C IV lines are both located at the same distance from the QSO central engine (~ 850 light days for APM 08279+5255).

The RM time lags can be also estimated by fitting with JAVELIN the LCs of multiple emission lines together. This is particularly useful when the LC sampling is sparse, since, if all emission lines follow the same variability model as the continuum, the available information to fit the variability increases. Therefore, we perform this analysis with the full data set of 138 continuum points and 30 points for each emission line, for a total of $N_{\text{tot}} = 198$ light-curve points to fit the eight parameters (continuum damping time scale and variability amplitude, two top-hat lags, two smoothing widths and two scale factors) of the DRW plus top-hat transfer function model of quasar line-to-continuum variability.

The joint fit with JAVELIN gives $t_{\text{lag}}^{\text{JAV}}(\text{Si IV}) = 4286^{+260}_{-417}$ days in the observer frame and $t_{\text{lag}}^{\text{JAV}}(\text{C IV}) = 4425^{+280}_{-560}$ days respectively. In Fig. 3, we show the posterior distribution of a JAVELIN MCMC run with $1.6 \cdot 10^5$ iterations for these time lags. Also, in Fig. 4 we show the emission-line LCs of Si IV and C IV scaled to the *R*-band continuum, and shifted back in time of the relevant RM lags. At a first glance, the emission-line LCs are both consistent with the interpolated decrease in the continuum flux after the rise around MJD $\sim 51,500$ observed by Lewis et al. (1999).

Some caution must be adopted in interpreting the result, since the lag associated to the cross-correlation peak corresponds to a maximum of the emission-line LCs just falling in a gap of the continuum LC (see Fig. 4). This is however made possible by the assumption of the method, which uses the information of the emission-line LCs to interpolate the continuum. In the continuum LC gap between 51,500 and 52,500 days, JAVELIN is therefore using the local maximum of the emission-line LCs at MJD $\sim 56,000$: although this is the probable cause of the extension at large time lags of the emission-line lag posterior distribution, and consequently of the asymmetric errors at 95% probability in the lag estimate (see Fig. 3), the result is quite plausible. With this measurement, APM 08279+5255 becomes the most distant object, and one of the intrinsically most luminous, for which RM time lags are available.

3.2. Reverberation mapping with the CCFs

For comparison with the time lags found by JAVELIN, also a CCF analysis of APM 08279+5255 line and continuum LCs is presented. The results are shown in Fig. 5: a peak in the ZDCF appears at $t_{\text{lag}}^{\text{ZDCF}} = 4095^{+867}_{-369}$ days in the observer frame, simultaneously for the Si IV and C IV. However, this peak is located in the last significant ZDCF bin, i.e. a bin containing at least the minimal number of points required to compute a statistically significant ZDCF value. The ZDCF point at a longer lag is already not significant. Coupled with the large bin width of the ZDCF peak, this prevents to compute the 68% probability confidence interval on the peak position over more than one ZDCF bin.

We evaluate t_{lag} from the ICCF estimating the lag uncertainty with the FR/RSS method: we obtain $t_{\text{lag}}^{\text{ICCF}}(\text{Si IV}) = 4114^{+1414}_{-983}$ days in the observer frame, and $t_{\text{lag}}^{\text{ICCF}}(\text{C IV}) = 4482^{+1036}_{-1414}$ days. We also quantify the significance of the CCF peaks by performing a Student's *t*-test (Bevington 1969; see also Shen et al. 2015), which allows to evaluate the integral probability of the null hypothesis $P(> r, N)$ for a correlation coefficient r computed over N pairs of data points. We compute this probability for both the ICCFs and ZDCFs: for the ICCFs, we obtain $P(> r, N) = 0.03$ for the Si IV ($r = 0.60$, $N = 12$) and 0.05 for the C IV ($r = 0.55$, $N = 12$) respectively; for the ZDCFs, the test gives $P(> r, N) = 0.04$ for the Si IV ($r = 0.53$, $N = 15$) and 0.29 for the C IV ($r = 0.21$, $N = 15$). As expected, the CCFs do not provide a statistically significant result; however, the peaks are all located close to the same position obtained with JAVELIN, indicating that the previously found lags are not an artifact of the adopted model.

4. Update of the C IV absorption variability

The variability of APM 08279+5255 C IV absorption features was presented in Paper I and Saturni et al. (2014). In the present paper, we take advantage of the new observations from the Loiano observatory and the photometric data set from the

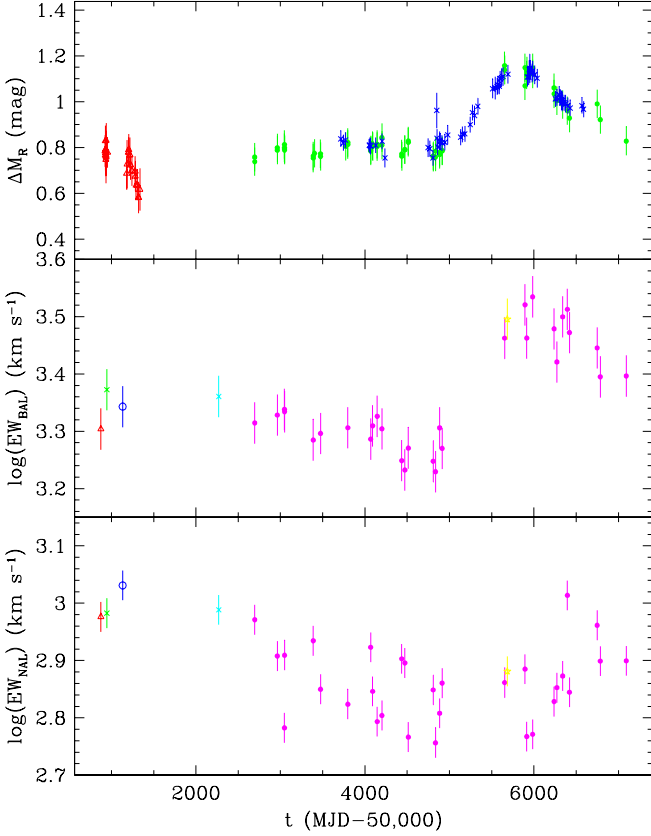


Fig. 6. *Upper panel:* updated time series of APM 08279+5255 *R*-band differential magnitude with 1σ errors, adding all the photometric data available in literature (same colour code than in the upper panel of Fig. 2). *Middle panel:* BAL EWs computed for all the existing APM 08279+5255 spectra with 1σ errors. *Lower panel:* NAL EWs computed for all the existing APM 08279+5255 spectra with 1σ errors. In both middle and lower panel, the Irwin et al. 1998 (red triangle), the Ellison et al. 1999 (green cross), the Hines et al. 1999 (blue circle), the Lewis et al. 2002 (cyan square) and the Saturni et al. 2015 (yellow star) spectra are all included along with the Asiago and Loiano spectra (magenta dots).

Catalina Sky Survey to extend the absorption variability monitoring in time, and partially fill the gaps in our time series. The data reduction is identical to that performed in Paper I. Fig. 6 shows the update of the C IV absorption equivalent width (EW) variability of APM 08279+5255 up to MJD = 57,093.

In Paper I, we have identified four absorption systems in the C IV region of APM 08279+5255, thanks to the availability of high-resolution spectra. We therefore distinguish two BAL components (respectively labeled BAL₁ and BAL₂ in Fig. 1) separated by a NAL system (“blue NAL” in Fig. 1) described in Srianand & Petitjean (2000). Another NAL system (“red NAL” in Fig. 1) is located redwards the C IV emission (Srianand & Petitjean 2000; Ellison et al. 2004). With respect to the previous variability analysis, the “blue NAL” has not been included in this update, due to the uncertainty in determining the residual contamination of its EW after the subtraction of the two BAL components. We describe the behaviour of the BAL troughs and the “red” NAL in the following subsections.

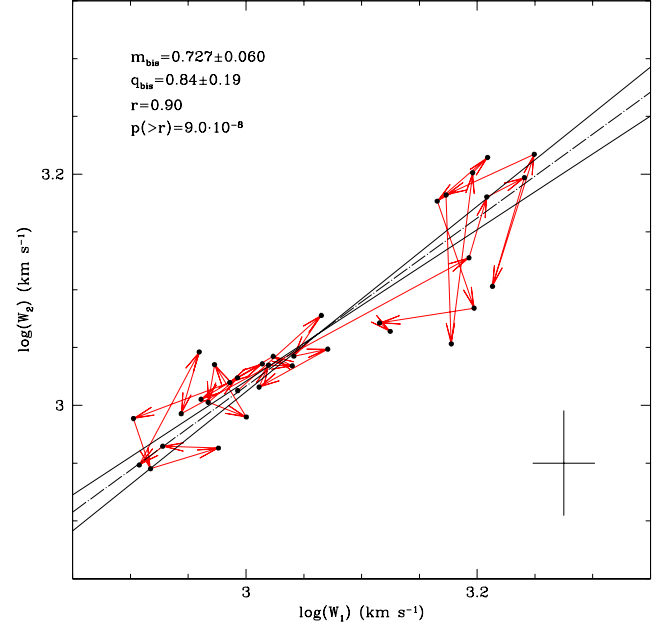


Fig. 7. EWs of the two C IV BAL troughs of APM 08279+5255, plotted one versus the other (black points). The red arrows connect consecutive epochs of EW pairs. The two correlation fits of BAL₁ versus BAL₂ and vice versa are shown (solid lines), along with the corresponding bisector fit (dot-dashed line). Slope m_{bis} and intercept q_{bis} of such fit, correlation coefficient r and corresponding null-hypothesis probability $p(>r)$ are reported. The cross in the right-lower corner represents the mean error on the data set in each direction.

4.1. The BAL variability

As described in Paper I and Saturni et al. (2014), we considered the sum of the two C IV BAL components as a single absorption feature for the purpose of the EW variability analysis. This was done since the EWs of such components, computed separately by modeling the BAL profile at low resolution with two Gaussian absorptions, vary in a highly correlated way over the whole monitoring time (see e.g. fig. 5 in Paper I). In order to verify that the new data do not change this result, we show in Fig. 7 that this correlation is maintained ($r = 0.90$, $p(>r) = 9.0 \cdot 10^{-8}$). This result is confirmed by computing the discrete cross-correlation function of the two BAL EWs according to the ZDCF algorithm introduced in Sect. 3, that peaks at $t_{lag} = 171^{+91}_{-513}$ days in the observer frame (35^{+19}_{-104} rest-frame days), which is consistent with no lag between the two components.

This simultaneous variability of different BAL troughs associated to different transitions (Brandt et al. 2014) or the same transition (Grier et al. 2015) is observed in some other BAL QSOs, indicating common physics driving the BAL variations. We quantify the comparison between BAL₁ and BAL₂ variability by performing a bisector fit (Akritas & Bershady 1996) of the relation between the logarithmic BAL EWs $\log W_1$ and $\log W_2$, obtaining:

$$\log W_2 = (0.727 \pm 0.060) \log W_1 + (0.84 \pm 0.19) \quad (4)$$

With respect to the simple correlation analyses among *R*-band magnitudes, BAL and NAL EWs presented in Paper I, in this paper we add the cross-correlation analyses. In order to do

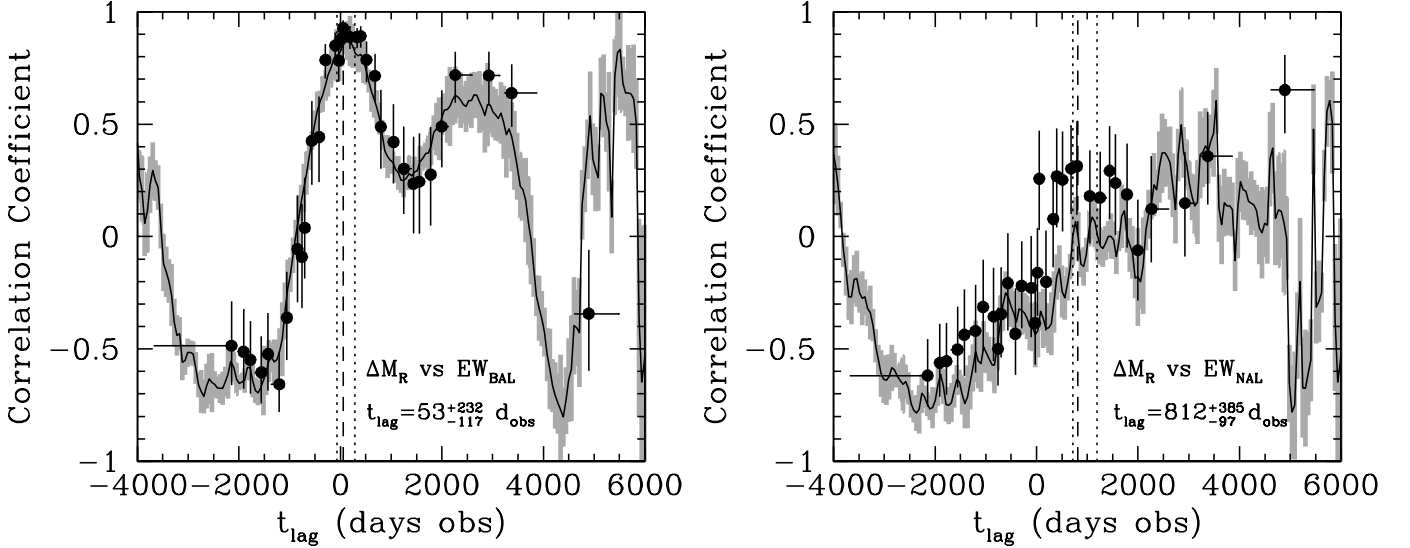


Fig. 8. *Left panel:* cross-correlation function of the R -band magnitudes with the total C IV BAL EW tracing the continuum. *Right panel:* cross-correlation function of the R -band magnitudes with the total C IV “red” NAL EW. In both panels, both the ICCF (black solid line), with 1σ errors in the y direction (grey bars), and ZDCF computed with 15 points per bin (black points), with 1σ errors in both x and y directions, are shown. The dashed vertical lines mark the delays of the most prominent peaks enclosed by their uncertainties at 68% probability (dotted lines), which are also numerically reported.

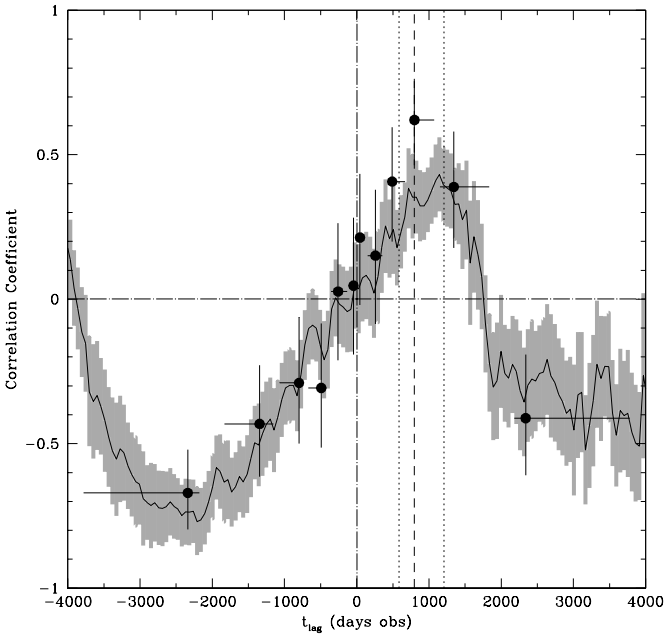


Fig. 9. Cross-correlation function of the BAL EW with the NAL EW variability. Both the ICCF (solid line), and the ZDCF computed with 20 points per bin (black dots), are shown with their respective 1σ errors. The ZDCF lag (dashed line) is indicated, along with its uncertainty at 68% probability (dotted lines).

this, we only apply the ICCF and ZDCF methods, since the reverberation model on which JAVELIN is based cannot be directly applied to absorption variability.

We present the results in the left panel of Fig. 8: as expected from a visual inspection of Fig. 6, the correlation peak appears at zero lag ($t_{\text{lag}} = 53^{+232}_{-117}$ days in the observer frame, with a

significance over 3σ level: $N = 15$, $r = 0.94$ and $P(> r, N) = 2 \cdot 10^{-7}$), since the absorbing gas lies along the line of sight and there is no light-travel lag between the continuum and absorption (Barlow et al. 1992; Barlow 1993). Nonetheless, a physical lag due to recombination time scale could be present, but is however short for high electron densities.

4.2. The NAL variability

At variance with the BAL behaviour, in Paper I and Saturni et al. (2014) the “red NAL” did not appear to show variations related to the strong continuum variation at MJD $\sim 55,000$. We argued that this could have been caused by a delayed variation in the ionisation state of the NAL absorber, not yet seen in the LC, with respect to the continuum changes. We estimated a lower limit to this physical recombination time lag of ~ 200 rest-frame days, roughly corresponding to the time span between MJD $\sim 55,000$ and $\sim 56,000$ in our data (see Fig. 6). With this limit, we placed an upper limit of $n_e \lesssim 2 \cdot 10^4 \text{ cm}^{-3}$ on the electron density of the absorber.

With the update of the NAL EW time series presented in Fig. 6, a delayed rise seems to appear with respect to the continuum variation of ~ 0.4 mag after MJD $\sim 55,000$, with the NAL EW rising by ~ 0.2 dex between MJD $\sim 56,000$ and $57,000$. At a glance, this would correspond to a rest-frame time lag of roughly 200 days. A measurement of this delay can provide a more robust estimate of the NAL electron density instead of the upper limit of Paper I.

We therefore compute the CCFs between the NAL EW and continuum variability. Both the ICCF and ZDCF are shown in the right panel of Fig. 8: at variance with the BAL case, here the correlation peak appears at different lags for ICCF (3541^{+1090}_{-2424} days in the observer frame) and ZDCF (812^{+385}_{-97} days), and both peaks are marginally significant at 2σ level ($N = 19$, $r = 0.60$, $P(> r, N) = 0.01$ for the ICCF; $N = 15$, $r = 0.65$, $P(> r, N) =$

Table 1. APM 08279+5255 relevant time lags.

Process	Obs-frame lag (days)	Rest-frame lag ^a (days)	Method
Si iv reverberation (single)	4095 ⁺⁸⁶⁷ ₋₃₆₉	834 ⁺¹⁷⁷ ₋₇₅	ZDCF
	4114 ⁺¹⁴¹⁴ ₋₉₈₃	838 ⁺²⁸⁸ ₋₂₀₀	ICCF
	4180 ⁺¹⁰³⁵ ₋₃₂₃	851 ⁺²¹¹ ₋₆₆	JAVELIN
C iv reverberation (single)	4095 ⁺⁸⁶⁷ ₋₃₆₉	834 ⁺¹⁷⁷ ₋₇₅	ZDCF
	4482 ⁺¹⁰³⁶ ₋₁₄₁₄	913 ⁺²¹¹ ₋₂₈₈	ICCF
	4243 ⁺³³⁷ ₋₃₅₅	863 ⁺⁶⁹ ₋₇₂	JAVELIN
Si iv reverberation (joint)	4286 ⁺²⁶⁰ ₋₄₁₇	873 ⁺⁵³ ₋₈₅	JAVELIN
C iv reverberation (joint)	4425 ⁺²⁸⁰ ₋₅₆₀	901 ⁺⁵⁷ ₋₁₁₄	JAVELIN
BAL ₁ vs BAL ₂ variability	171 ⁺⁹¹ ₋₅₁₃	35 ⁺¹⁹ ₋₁₀₄	ZDCF
BAL vs continuum variability	53 ⁺²³² ₋₁₁₇	11 ⁺⁴⁷ ₋₂₄	ZDCF
NAL vs BAL variability	799 ⁺⁴⁰⁸ ₋₂₁₄	163 ⁺⁸³ ₋₄₄	ZDCF
	1145 ⁺⁷⁴⁸ ₋₇₆₄	233 ⁺¹⁵² ₋₁₅₆	ICCF

^aThe rest-frame lag is computed with the systemic redshift $z = 3.911$.

0.01 for the ZDCF). Also a visual inspection of Fig. 6 shows that the identification of the main CCF peaks is not straightforward.

However, in Paper I we suggested that the absorption variability occurs in response to the variations in the *true* C iv ionising continuum at ~ 200 Å, which is not observed. The BAL variability is assumed to trace this ionising continuum with no or very small recombination lag due to a high electron density of the absorbing wind. Therefore, we assume the BAL EW time series as a proxy of the ionising continuum variability, and compute ICCF and ZDCF with the NAL EWs. The result is shown in Fig. 9: a single peak arises at $t_{lag} = 1145^{+748}_{-764}$ days in the observer frame for the ICCF and at $t_{lag} = 799^{+408}_{-214}$ days for the ZDCF, with a significance at more than 2σ level in both cases ($N = 26$, $r = 0.43$, $P(> r, N) = 0.02$ for the ICCF; $N = 20$, $r = 0.62$, $P(> r, N) = 3 \cdot 10^{-3}$ for the ZDCF). This favours the correlation between the continuum flux decrease beginning at MJD $\sim 55,000$ and the NAL EW rise after MJD $\sim 56,000$. Moreover, it suggests at the same time that the BAL variability is in fact a better proxy of the ionising continuum variations than the *R*-band continuum.

5. Discussion

Thanks to our long-time spectro-photometric monitoring of the high- z bright quasar APM 08279+5255, we have obtained several time lags linking the variability of emission and absorption lines to that of the driving continuum emission. In this way, we are able to probe (i) the region of the ionised gas clouds producing the emission lines, and (ii) the regions where the high-velocity outflows responsible of broad absorption in quasar spectra originate. In Tab. 1, we summarise all these time lags together, giving them both in the observer frame and in the rest frame for $z = 3.911$.

In this section, we discuss what can be inferred about the relevant physical parameters of these regions. From the Si iv and C iv emission-line lags, we can estimate the black hole mass of APM 08279+5255 with some assumptions on the BLR shape and inclination (which are summarised into the form factor f). From the C iv NAL recombination lag with respect to the ionising continuum at ~ 200 Å, we can obtain information about the electron density and the distance of the absorbing gas from the central engine.

5.1. Si iv and C iv BLR stratification

Since the time lags obtained for Si iv and for C iv are equal within errors, this means that the respective BLRs must be approximately located at the same distance from the central black hole. How does this compare with the BLR size ratio found in low-luminosity AGNs? In order to explore this point, we collected from the literature all the objects having RM time lags of both Si iv and C iv. These objects are the Seyfert galaxies NGC 3783, NGC 5548 and NGC 7469 (Peterson et al. 2004).

In Fig. 10 we show such collection of rest-frame time lags from Si iv as a function of those from C iv, and perform a logarithmic bisector fit to the data in order to quantify the average size difference between Si iv and C iv BLRs from Seyfert galaxies to quasars, spanning three orders of magnitude of BLR size. Allowing both slope and intercept to vary, the fit indicates a possible increase of the time lag ratio, and hence of the BLR size ratio, with a power-law behaviour with logarithmic slope 1.10 ± 0.03 . For comparison, a fit with a unitary slope is also shown in Fig. 10, corresponding to an average ratio $\langle R_{BLR}^{SiIV} / R_{BLR}^{CIV} \rangle = \langle t_{lag}^{SiIV} / t_{lag}^{CIV} \rangle = 0.72^{+0.10}_{-0.08}$. This result is dominated by the Seyfert galaxies, whose average ratio is $\langle R_{BLR}^{SiIV} / R_{BLR}^{CIV} \rangle = 0.69^{+0.11}_{-0.10}$.

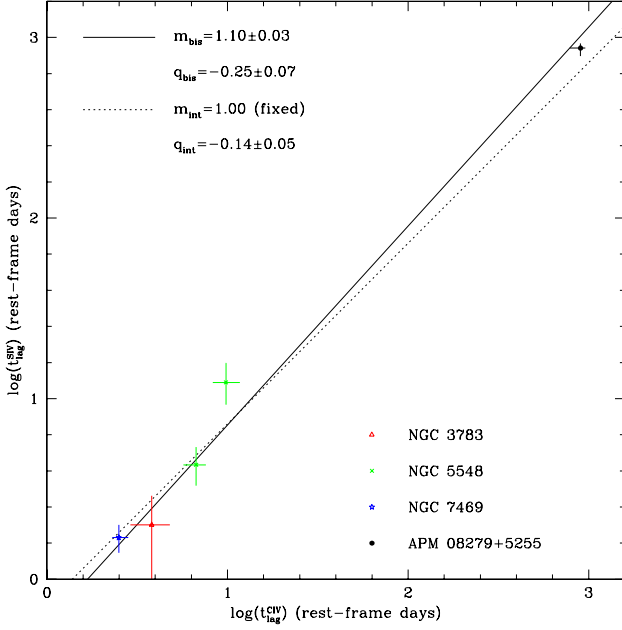


Fig. 10. Rest-frame Si IV time lags as a function of C IV lags. All the available data from the literature are shown, together with our measurements from the RM of APM 08279+5255 (legend is on the plot). For the whole data set, both a free linear fit in the logarithmic space (*solid line*), and a linear fit with logarithmic slope fixed to unity (*dotted line*), have been performed. Fit coefficients are indicated in the plot with their 1σ errors.

5.2. The size-luminosity relation for the C IV BLR

Our result for APM 08279+5255 allows us to extend the size-luminosity relation for the C IV emitting region up to $\sim 10^{48}$ erg s $^{-1}$ in monochromatic luminosity at 1350 Å $\lambda L_{\lambda}(1350)$. In Fig. 11 we collect all the available data for the size of the C IV emitting region in AGNs as a function of their $\lambda L_{\lambda}(1350)$, where we add our point for APM 08279+5255 to spectroscopic RM measurements (Peterson et al. 2004, 2005; Metzroth et al. 2006; Kaspi et al. 2007; Perna et al. 2014; Trevese et al. 2014). Also, we add the point for the quasar MACHO 13.6805.324 obtained with photometric RM by Chelouche et al. (2012), and the point for the gravitationally lensed quasar QSO 2237+0305 obtained through microlensing by Sluse et al. (2011).

We fit a power-law relation $R_{BRL} \propto L_{1350}^{\beta}$ to this data set with a method that takes into account the uncertainties in both variables and the intrinsic scatter of points. We run a high number of bisector fits (Akritas & Bershady 1996) on data sets in which each original point is replaced by casting a pair of substituting values within the associated error box; these values are weighted by an asymmetric distribution function, represented by two demi-Gaussian distributions with different standard deviations, corresponding to the asymmetric uncertainties. The best-fit relation obtained with 10^4 runs is:

$$\log R_{BRL} = (0.9 \pm 0.7) + (0.54 \pm 0.02) \log \left[\frac{\lambda L_{\lambda}(1350)}{10^{44} \text{ erg s}^{-1}} \right] \quad (5)$$

With respect to previous relations (Peterson et al. 2005; Kaspi et al. 2007), having added objects with uncertain luminosities to the fit gives a large error in the intercept. In the two cases of the quasars PG 1247+267 and APM 08279+5255, this

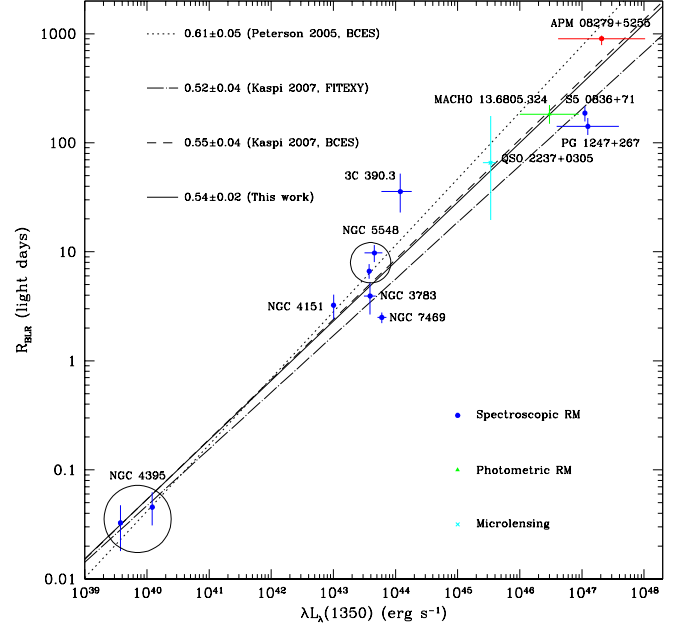


Fig. 11. Size-luminosity relation for C IV BLR. Together with APM 08279+5255, all the objects with measurements of C IV BLR size and monochromatic luminosity at 1350 Å available in the literature have been included in this plot: NGC 4395, NGC 7469, NGC 3783, NGC 5548 and 3C 390.3 from Peterson et al. (2004, 2005), NGC 4151 from Metzroth et al. (2006), QSO 2237+0305 from Sluse et al. (2011), MACHO 13.6805.324 from Chelouche et al. (2012), S5 0836+71 from Kaspi et al. (2007) and PG 1247+267 from Perna et al. (2014); Trevese et al. (2014). Colour and symbol codes are explained in the plot. For comparison with our fit, also the fits performed by Peterson et al. (2005, 2006) and Kaspi et al. (2007) are reported (see legend in the plot).

is due to the unknown lens magnification factor μ . In fact, as described in Trevese et al. (2014), the first object has relatively small emission-line widths with respect to its luminosity, an Eddington ratio of ~ 10 , and a significant deviation from the $\alpha_{OX} - L_{2500}$ relation (Shemmer et al. 2014): an invisible gravitational lens with $\mu \approx 10$ could explain at once all the anomalies described in Trevese et al. (2014). For APM 08279+5255, instead, the fact that the lensing galaxy is not visible (Lewis et al. 2002) leads to very model-dependent estimates of the magnification factor. Currently, μ ranges between ~ 100 (Egami et al. 2000) and ~ 4 (Riechers et al. 2009) for APM 08279+5255; therefore, in order to provide a rough indication of the global uncertainty due to both the statistical errors and the ignorance of the lens magnification, we adopt as uncertainty in the quasar luminosity the whole range of plausible $\lambda L_{\lambda}(1350)$ between $\mu = 4$ and 100 for APM 08279+5255, and the range between $\mu = 1$ (i.e. no magnification) and 10 for PG 1247+267.

5.3. APM 08279+5255 black hole mass estimates

In order to give a direct estimate of the black hole mass of APM 08279+5255, we follow the approach of Trevese et al. (2014). Therefore, we first identify the velocity Δv appearing in Eq. 1 with the rms velocity dispersion along the line of sight σ_l . We then compute the uncertainty on σ_l for Si IV by applying the

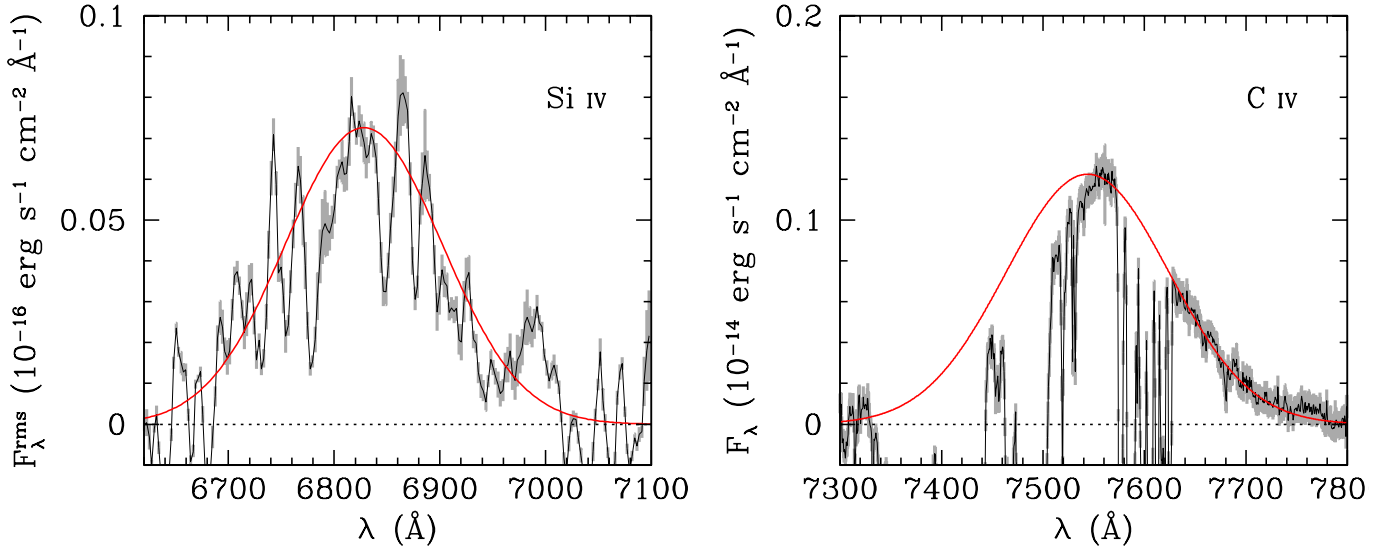


Fig. 12. *Left panel:* continuum-subtracted rms spectrum of APM 08279+5255 Si IV emission line from our RM monitoring. *Right panel:* continuum-subtracted HST spectrum of the C IV emission line. In both panels, errors on the flux level (grey bars) and best-fit Gaussians (red curves) are shown. For Si IV, the major deviations from the best-fit curve are the residuals of intrinsic narrow absorptions superimposed to the emission line, as can be seen from the analysis by Srianand & Petitjean (2000) and Ellison et al. (2004).

bootstrap method described in Peterson et al. (2004), obtaining $\Delta v_{SiIV} = 3245^{+101}_{-107}$ km s⁻¹; the use of σ_l both avoids underestimates of Δv caused by narrow emission-line components and the effect of non-virial outflows varying on time scales longer than RM lags (e.g., Denney 2012).

Unfortunately, we cannot apply the same procedure to C IV, since its emission-line profile is heavily affected by absorption features that prevent to compute a reliable rms spectrum in that region. Therefore, instead of using σ_l , for C IV we adopt the standard deviation of a Gaussian profile $\sigma_g = 3200 \pm 30$ km s⁻¹, as measured through the C IV emission profile fit performed on the high-resolution dereddened HST/STIS spectrum of APM 08279+5255. Since the unabsorbed spectral intervals in this spectrum appear to be free of narrow components and outflows in emission, we can consider this as a good equivalent estimate of the proper C IV rms σ_l . In Fig. 12, we show both the fit of C IV on the HST spectrum and a Gaussian fit of the rms Si IV, performed by only allowing the rms line amplitude to vary, setting the peak wavelength to λ_{1400} Å at $z = 3.87$ (Irwin et al. 1998; Downes et al. 1999) and the line width to the Si IV σ_l .

Finally, we multiply the posterior distributions of t_{lag} for Si IV and C IV for the respective statistical distributions of Δv^2 to obtain two posterior distributions of APM 08279+5255 virial products $t_{lag}\Delta v^2$, to be inserted in Eq. 1 in order to obtain the black hole mass M_{BH} . We adopt as form factor the value $f = 5.5$, obtained by Onken et al. (2004) through the calibration of the H β RM masses on the relation between black hole masses and stellar velocity dispersions in galaxy bulges (Ferrarese & Merritt 2000; Merritt & Ferrarese 2001b; Gültekin et al. 2009), which is appropriate for the definition of $\Delta v = \sigma_l$ (not FWHM); although more recent estimates provide different values for f (e.g., Pancoast et al. 2014 and refs. therein), we choose this commonly used value for a direct comparison with the literature nonetheless, as also done in Trevese et al. (2014). Fig. 13 shows such distributions, that give an identical result of $M_{BH} = (1.00^{+0.17}_{-0.13}) \cdot 10^{10} M_{\odot}$ as best estimate of the virial mass.

5.4. Estimate of the lens magnification

APM 08279+5255 is a well-known gravitational lens, first confirmed case with an odd number of images of the lensed source and no observed trace of the lensing galaxy (Lewis et al. 2002). Therefore, the estimate of the lens magnification μ only relies on modeling the lensed quasar image from high-resolution optical/infrared imaging, and the values of μ are significantly discrepant when estimated from different lens models (Egami et al. 2000; Riechers et al. 2009). This primarily affects the single-epoch black hole mass estimates from mass-luminosity virial relationships, that can give differences in the value of M_{BH} of up to one order of magnitude when adopting such magnifications.

Our direct RM measurement of the C IV R_{BLR} for APM 08279+5255 allows us to invert the relation between the BLR size and UV luminosity, thus giving a model-independent estimate of μ that can discriminate between the competing models. We thus solve eq. 3 of Kaspi et al. (2007) for $\lambda L_{\lambda}(1350)$, which is not affected by our ignorance on APM 08279+5255 true luminosity, adopting our fiducial JAVELIN time lag for C IV of 901 days in the rest frame:

$$\lambda L_{\lambda}^{true}(1350) = 10^{42.56} R_{BLR}^{1.92} = (1.7^{+6.6}_{-1.2}) \cdot 10^{48} \text{ erg s}^{-1} \quad (6)$$

With a measured luminosity $\lambda L_{\lambda}^{meas}(1350) = 4.13 \cdot 10^{48}$ erg s⁻¹ from our de-reddened spectra, the lens magnification can be estimated by:

$$\mu = \frac{\lambda L_{\lambda}^{meas}(1350)}{\lambda L_{\lambda}^{true}(1350)} = 2.4^{+5.8}_{-1.9} \quad (7)$$

Although affected by large errors, due to the uncertainty on the BLR-luminosity relation, such a low magnification favours the lens model by Riechers et al. (2009) with respect to that by Egami et al. (2000).

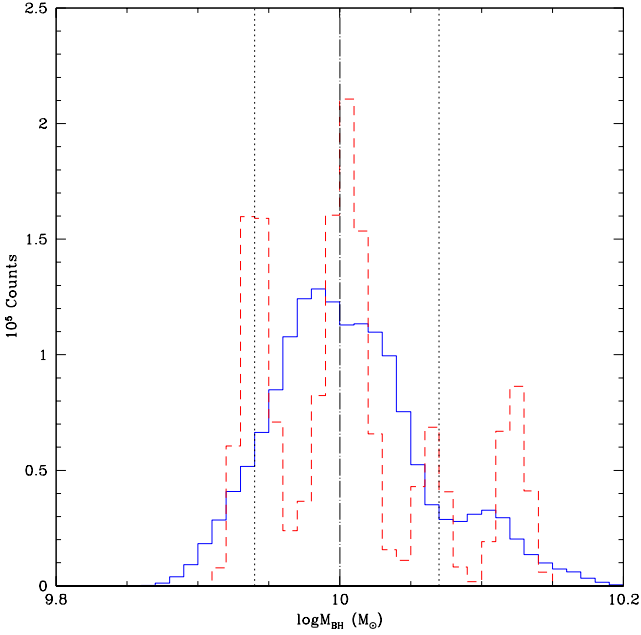


Fig. 13. Posterior distribution of APM 08279+5255 black hole mass from Si IV (blue solid histogram) and C IV (red dashed histogram) RM. The best estimate of the black hole mass (dot-dashed line) is indicated together with its confidence intervals at 68% probability (dotted lines).

5.5. Black hole mass versus host-galaxy mass: an overmassive black hole for APM 08279+5255

Having measured the black hole mass of APM 08279+5255, we now address the question of how it compares with the mass of the host galaxy. From the known relation between black hole mass and host-galaxy bulge mass for nearby galaxies (Magorrian et al. 1998; Merritt & Ferrarese 2001a; Marconi & Hunt 2003; Häring & Rix 2004), the expected bulge mass M_{bulge} for APM 08279+5255 would be ~ 400 times M_{BH} ; from CO emission-line structure, Riechers et al. (2009) derived $M_{bulge} = 3.0 \cdot 10^{11} / \mu M_{\odot}$, that corresponds to $7.5 \cdot 10^{10} M_{\odot}$ for $\mu = 4$. Using our RM measurement of M_{BH} , this means that $M_{bulge} = 7.5 M_{BH}$ for APM 08279+5255, slightly higher than Riechers et al. (2009) estimate but still more than 50 times lower than the value extrapolated from the local $M_{bulge} - M_{BH}$ ratio.

This revised result confirms the conclusions by Riechers et al. (2009), i.e. a black-hole mass assembly already ended at very early cosmic times into a galaxy that has still to form the largest part of its stars. A handful of other objects presenting a similar $M_{BH}/M_{bulge} \sim 0.1$ are known so far (Walter et al. 2004; Riechers et al. 2008a,b), APM 08279+5255 being the first one with a direct estimate of its M_{BH} . High M_{BH}/M_{bulge} ratios may be common at high redshift, with a non-evolving black hole-to-total stellar mass ratio (M_{BH}/M_*) as stars later settle into galaxy bulges and a M_{BH}/M_{bulge} ratio at $z \sim 0$ (e.g., Jahnke et al. 2009).

The value of M_* for APM 08279+5255 is currently unknown; still, we note that, in the $M_{BH} - M_*$ diagram (see fig. 2 of Trakhtenbrot et al. 2015), APM 08279+5255 hosts one of the most massive black holes measured so far. Its M_{BH} is in fact slightly higher than CID-947, a $z \sim 3.3$ quasar interpreted as a possible prototype of a class of objects with still largely incomplete star formation in the host galaxy (Trakhtenbrot et al. 2015).

5.6. Physics and location of the C IV absorbing gas

We argued in Paper I that the most plausible mechanism for absorption variability in APM 08279+5255 is a change in the photo-ionisation state of the gas driven by the variability of the ionising continuum. Within this framework, the increase in the absorption EWs after the flux drop at MJD $\sim 55,000$ is due to an equivalent increase in the density of C IV ions, through the recombination process $C^{4+} \rightarrow C^{3+}$. The time scales obtained through the CCF between the absorption and continuum variability measure the delay between a variation in the quasar radiation field and the corresponding variation in the density of the absorbing ions, through which we can infer the density of the absorbing gas, and thus its distance from the central engine, or at least a lower limit.

Since the change in the BAL EW is simultaneous with the *R*-band strong continuum variation, the time lag obtained for the main C IV broad absorption features is compatible with zero. Thus, we cannot establish a significant lower limit to the electron density of the BAL wind.

Conversely, the observed lag in the NAL EW variability can give an estimate of the density of the absorbing clouds n_e . Assuming $\alpha_{rec} = 2.8 \cdot 10^{-12} \text{ cm}^3 \text{ s}^{-1}$ (Arnaud & Rothenflug 1985) as the recombination coefficient of C^{4+} atoms, we compute the value of n_e as follows:

$$n_e = \frac{1}{t_{lag} \alpha_{rec}} = (2.5^{+1.0}_{-0.8}) \cdot 10^4 \text{ cm}^{-3}, \quad (8)$$

assuming the ZDCF lag computed with respect to the BAL variability (see Sect. 4.2) as an estimate of the NAL recombination time lag.

A rough estimate of the distance of the NAL gas from the continuum source may be obtained through the knowledge of the ionisation parameter U of APM 08279+5255, which is linked to the distance from the ionising source and to its luminosity by (e.g., Peterson 1997):

$$U = \frac{1}{4\pi r^2 c n_e} \int_{\nu_{ion}}^{+\infty} \frac{L_{\nu}}{h\nu} d\nu \quad (9)$$

We can derive r as:

$$r_{NAL} = \sqrt{\frac{1}{4\pi U c n_e} \int_{\nu_{ion}}^{+\infty} \frac{L_{\nu}}{h\nu} d\nu}, \quad (10)$$

where we adopt $U \sim 10^{-2}$ from Srianand & Petitjean (2000). In order to estimate L_{ν} over the range of (unobserved) ionising energies, we follow the procedure of Grier et al. (2015), calibrating the synthetic quasar spectral energy distribution (SED) of Dunn et al. (2010) to APM 08279+5255 bolometric luminosity $L_{bol} \sim 4.5 \cdot 10^{48} \text{ erg s}^{-1}$. Such luminosity is inferred from the observed flux density at 3000 \AA of the optical/IR spectrum of APM 08279+5255 taken at the Telescopio Nazionale Galileo (La Palma, Canarian Islands; Saturni et al., in prep.), with a bolometric correction factor of 5 (Richards et al. 2006) and the lens magnification $\mu = 4$ of Riechers et al. (2009); with this normalisation, we compute $\int_{\nu_{ion}}^{+\infty} (L_{\nu}/h\nu) d\nu = 8.2 \cdot 10^{58} \text{ s}^{-1}$ for energies of up to 50 keV. Substituting these quantities in Eq. 10, we finally obtain $r_{NAL} \approx 9.6 \text{ kpc}$, compatible with a location of the NAL absorbers in the body of APM 08279+5255 host galaxy.

6. Conclusions

We can summarise our results as follows.

1. The long monitoring of APM 08279+5255 obtained by combining our observational campaign with literature data, with a total sample of 138 photometric *R*-band points and 30 spectra (plus 5 from the literature, used for the study on the C iv absorption variability) spanning ~ 16 years in the observer frame (~ 3.5 years in the rest frame), allowed us to perform the RM of this quasar. The resulting rest-frame time lag is of ~ 900 days in the rest frame for both Si iv and C iv.
2. We find $t_{lag}^{SiIV}/t_{lag}^{CIV} \sim 1$ for APM 08279+5255. This ratio is only marginally consistent with the average value found for Seyfert galaxies ($\langle t_{lag}^{SiIV}/t_{lag}^{CIV} \rangle = 0.7 \pm 0.1$), thus possibly indicating a slight increase of $t_{lag}^{SiIV}/t_{lag}^{CIV}$ from Seyferts to quasars.
3. We update the distance-luminosity relation for quasars obtained through C iv lags (Peterson et al. 2005; Kaspi et al. 2007), and compute a black hole mass of $\sim 10^{10} M_{\odot}$ for APM 08279+5255.
4. With our direct time lag measurement, we can invert the distance-luminosity relation for C iv of Kaspi et al. (2007) in order to obtain an estimate of APM 08279+5255 lens magnification, so far uncertain between 100 (Egami et al. 2000) and 4 (Riechers et al. 2009) depending on the model of the lensing galaxy shape, size and positioning. This provides an estimate of $\mu = 2.4^{+5.8}_{-1.9}$, consistent at 1σ level with the model of Riechers et al. (2009) and disfavouring the model of Egami et al. (2000) instead.
5. We revise the M_{BH}/M_{bulge} ratio presented by Riechers et al. (2009), confirming that APM 08279+5255 has an oversized black hole with respect to its host-galaxy bulge (Walter et al. 2004; Riechers et al. 2008a,b). A future measurement of its host-galaxy stellar mass would be extremely important in order to establish whether APM 08279+5255 host galaxy has an under-developed stellar component, in analogy with the case of CID-947 (Trakhtenbrot et al. 2015).
6. We update the study on the C iv absorption variability already presented in Paper I and Saturni et al. (2014), and further strengthen the hypothesis of BAL variations driven by changes in the C iv ionising continuum at $\sim 200 \text{ \AA}$.
7. At variance with the BAL components, the narrow absorption system redwards the C iv $\lambda 1549$ emission exhibits a variation delayed by ~ 160 days in the rest frame with respect to the ionising continuum. Under the assumption that this lag is due to $C^{+4} \rightarrow C^{+3}$ recombination, we estimate a distance of the NAL gas from the central engine consistent with galactic sizes.

Acknowledgements. We thank our anonymous referee for their helpful comments. We are also grateful to Ying Zu (McWilliams Center for Cosmology, Carnegie Mellon University) for the useful discussion about the use of JAVELIN. We acknowledge funding from PRIN/MIUR-2010 award 2010NHBSBE. M.D. acknowledges PRIN INAF 2011 funding. This research is based on observations collected at the Copernico telescope (Asiago, Italy) of the INAF-Osservatorio Astronomico di Padova, and at the Cassini Telescope (Loiano, Italy) of the INAF-Osservatorio Astronomico di Bologna.

References

Akritis, M. G. & Bershad, M. A. 1996, *ApJ*, 470, 706
 Alexander, T. 1997, in *Astrophysics and Space Science Library*, Vol. 218, *Astronomical Time Series*, ed. D. Maoz, A. Sternberg, & E. M. Leibowitz, 163
 Alexander, T. 2013, *ArXiv e-prints*
 Arnaud, M. & Rothenflug, R. 1985, *A&AS*, 60, 425

Barlow, T. A. 1993, PhD thesis, California University
 Barlow, T. A., Junkkarinen, V. T., Burbidge, E. M., et al. 1992, *ApJ*, 397, 81
 Bevington, P. R. 1969, *Data reduction and error analysis for the physical sciences* (New York: McGraw-Hill, 1969)
 Brandt, W. N., Filiz Ak, N., Hall, P. B., Schneider, D. P., & SDSS-III BAL Variability Team. 2014, in *American Astronomical Society Meeting Abstracts*, Vol. 223, *American Astronomical Society Meeting Abstracts #223*, #126.01
 Capellupo, D. M., Hamann, F., Shields, J. C., Halpern, J. P., & Barlow, T. A. 2013, *MNRAS*, 429, 1872
 Capellupo, D. M., Hamann, F., Shields, J. C., Rodríguez Hidalgo, P., & Barlow, T. A. 2011, *MNRAS*, 413, 908
 Capellupo, D. M., Hamann, F., Shields, J. C., Rodríguez Hidalgo, P., & Barlow, T. A. 2012, *MNRAS*, 422, 3249
 Cattaneo, A., Faber, S. M., Binney, J., et al. 2009, *Nature*, 460, 213
 Chelouche, D., Daniel, E., & Kaspi, S. 2012, *ApJ*, 750, L43
 Denney, K. D. 2012, *ApJ*, 759, 44
 Downes, D., Neri, R., Wiklind, T., Wilner, D. J., & Shaver, P. A. 1999, *ApJ*, 513, L1
 Drake, A. J., Djorgovski, S. G., Mahabal, A., et al. 2009, *ApJ*, 696, 870
 Dunn, J. P., Bautista, M., Arav, N., et al. 2010, *ApJ*, 709, 611
 Edelson, R. A. & Krolik, J. H. 1988, *ApJ*, 333, 646
 Egami, E., Neugebauer, G., Soifer, B. T., et al. 2000, *ApJ*, 535, 561
 Ellison, S. L., Ibata, R., Pettini, M., et al. 2004, *A&A*, 414, 79
 Ellison, S. L., Lewis, G. F., Pettini, M., et al. 1999, *PASP*, 111, 946
 Elvis, M. 2000, *ApJ*, 545, 63
 Ferrarese, L. & Merritt, D. 2000, *ApJ*, 539, L9
 Filiz Ak, N., Brandt, W. N., Hall, P. B., et al. 2013, *ApJ*, 777, 168
 Gaskell, C. M. & Peterson, B. M. 1987, *ApJS*, 65, 1
 Gibson, R. R., Brandt, W. N., Schneider, D. P., & Gallagher, S. C. 2008, *ApJ*, 675, 985
 Grier, C. J., Hall, P. B., Brandt, W. N., et al. 2015, *ArXiv e-prints*
 Gültekin, K., Richstone, D. O., Gebhardt, K., et al. 2009, *ApJ*, 698, 198
 Hall, P. B., Anosov, K., White, R. L., et al. 2011, *MNRAS*, 411, 2653
 Häring, N. & Rix, H.-W. 2004, *ApJ*, 604, L89
 Hines, D. C., Schmidt, G. D., & Smith, P. S. 1999, *ApJ*, 514, L91
 Irwin, M. J., Ibata, R. A., Lewis, G. F., & Totten, E. J. 1998, *ApJ*, 505, 529
 Jahnke, K., Bongiorno, A., Brusa, M., et al. 2009, *ApJ*, 706, L215
 Kaspi, S., Brandt, W. N., Maoz, D., et al. 2007, *ApJ*, 659, 997
 Kaspi, S., Smith, P. S., Netzer, H., et al. 2000, *ApJ*, 533, 631
 Kelly, B. C., Bechtold, J., & Siemiginowska, A. 2009, *ApJ*, 698, 895
 Kozłowski, S., Kochanek, C. S., Udalski, A., et al. 2010, *ApJ*, 708, 927
 Krongold, Y., Binette, L., & Hernández-Ibarra, F. 2010, *ApJ*, 724, L203
 Lewis, G. F., Ibata, R. A., Ellison, S. L., et al. 2002, *MNRAS*, 334, L7
 Lewis, G. F., Robb, R. M., & Ibata, R. A. 1999, *PASP*, 111, 1503
 Lundgren, B. F., Willite, B. C., Brunner, R. J., et al. 2007, *ApJ*, 656, 73
 Lynds, C. R. 1967, *ApJ*, 147, 396
 MacLeod, C. L., Ivezić, Ž., Kochanek, C. S., et al. 2010, *ApJ*, 721, 1014
 Magorrian, J., Tremaine, S., Richstone, D., et al. 1998, *AJ*, 115, 2285
 Marconi, A. & Hunt, L. K. 2003, *ApJ*, 589, L21
 McLure, R. J. & Dunlop, J. S. 2004, *MNRAS*, 352, 1390
 Merritt, D. & Ferrarese, L. 2001a, *MNRAS*, 320, L30
 Merritt, D. & Ferrarese, L. 2001b, *ApJ*, 547, 140
 Metzroth, K. G., Onken, C. A., & Peterson, B. M. 2006, *ApJ*, 647, 901
 Netzer, H. 2003, *ApJ*, 583, L5
 Onken, C. A., Ferrarese, L., Merritt, D., et al. 2004, *ApJ*, 615, 645
 Pancoast, A., Brewer, B. J., Treu, T., et al. 2014, *MNRAS*, 445, 3073
 Pei, Y. C. 1992, *ApJ*, 395, 130
 Perna, M., Trevese, D., Vagnetti, F., & Saturni, F. G. 2014, *Advances in Space Research*, 54, 1429
 Peterson, B. M. 1993, *PASP*, 105, 247
 Peterson, B. M. 1997, *An Introduction to Active Galactic Nuclei (An introduction to active galactic nuclei, Publisher: Cambridge, New York Cambridge University Press, 1997 Physical description xvi, 238 p. ISBN 0521473489)*
 Peterson, B. M., Bentz, M. C., Desroches, L.-B., et al. 2005, *ApJ*, 632, 799
 Peterson, B. M., Bentz, M. C., Desroches, L.-B., et al. 2006, *ApJ*, 641, 638
 Peterson, B. M., Ferrarese, L., Gilbert, K. M., et al. 2004, *ApJ*, 613, 682
 Peterson, B. M., Wanders, I., Horne, K., et al. 1998, *PASP*, 110, 660
 Petitjean, P., Aracil, B., Srianand, R., & Ibata, R. 2000, *A&A*, 359, 457
 Press, W. H., Rybicki, G. B., & Hewitt, J. N. 1992, *ApJ*, 385, 416
 Richards, G. T., Lacy, M., Storrie-Lombardi, L. J., et al. 2006, *ApJS*, 166, 470
 Riechers, D. A., Walter, F., Brewer, B. J., et al. 2008a, *ApJ*, 686, 851
 Riechers, D. A., Walter, F., Carilli, C. L., Bertoldi, F., & Momjian, E. 2008b, *ApJ*, 686, L9
 Riechers, D. A., Walter, F., Carilli, C. L., & Lewis, G. F. 2009, *ApJ*, 690, 463
 Röser, S., Demleitner, M., & Schilbach, E. 2010, *AJ*, 139, 2440
 Rybicki, G. B. & Kleyna, J. T. 1994, in *Astronomical Society of the Pacific Conference Series*, Vol. 69, *Reverberation Mapping of the Broad-Line Region*

- in *Active Galactic Nuclei*, ed. P. M. Gondhalekar, K. Horne, & B. M. Peterson, 85
- Rybicki, G. B. & Press, W. H. 1992, *ApJ*, 398, 169
- Salpeter, E. E. 1964, *ApJ*, 140, 796
- Saturni, F. G., Trevese, D., Vagnetti, F., & Perna, M. 2014, *Advances in Space Research*, 54, 1434
- Shemmer, O., Brandt, W. N., Paolillo, M., et al. 2014, *ApJ*, 783, 116
- Shen, Y., Brandt, W. N., Dawson, K. S., et al. 2015, *ApJS*, 216, 4
- Shen, Y., Richards, G. T., Strauss, M. A., et al. 2011, *ApJS*, 194, 45
- Sluse, D., Schmidt, R., Courbin, F., et al. 2011, *A&A*, 528, A100
- Srianand, R. & Petitjean, P. 2000, *A&A*, 357, 414
- Trakhtenbrot, B., Urry, C. M., Civano, F., et al. 2015, *ArXiv e-prints*
- Trevese, D., Paris, D., Stirpe, G. M., Vagnetti, F., & Zitelli, V. 2007, *A&A*, 470, 491
- Trevese, D., Perna, M., Vagnetti, F., Saturni, F. G., & Dadina, M. 2014, *ApJ*, 795, 164
- Trevese, D., Saturni, F. G., Vagnetti, F., et al. 2013, *A&A*, 557, A91
- Turnshek, D. A. 1988, in *QSO Absorption Lines: Probing the Universe*, ed. J. C. Blades, D. A. Turnshek, & C. A. Norman, 17
- Urry, C. M. & Padovani, P. 1995, *PASP*, 107, 803
- Vestergaard, M. & Peterson, B. M. 2006, *ApJ*, 641, 689
- Walter, F., Carilli, C., Bertoldi, F., et al. 2004, *ApJ*, 615, L17
- Wandel, A., Peterson, B. M., & Malkan, M. A. 1999, *ApJ*, 526, 579
- Welsh, W. F. 1999, *PASP*, 111, 1347
- Weymann, R. & Foltz, C. 1983, in *Liege International Astrophysical Colloquia*, Vol. 24, *Liege International Astrophysical Colloquia*, ed. J.-P. Swings, 538–555
- White, R. J. & Peterson, B. M. 1994, *PASP*, 106, 879
- Zel'dovich, Y. B. & Novikov, I. D. 1965, *Soviet Physics Doklady*, 9, 834
- Zu, Y., Kochanek, C. S., Kozłowski, S., & Udalski, A. 2013, *ApJ*, 765, 106
- Zu, Y., Kochanek, C. S., & Peterson, B. M. 2011, *ApJ*, 735, 80

Table 2. APM 08279+5255 continuum and emission-line fluxes.

MJD–50,000 (days)	Telescope	Obs Type	F_Q/F_S	$F_{\text{SiIV}} (10^{-13} \text{ erg s}^{-1} \text{ cm}^{-2})$	$F_{\text{CIV}} (10^{-13} \text{ erg s}^{-1} \text{ cm}^{-2})$
925.0	V ¹	P ^a	0.485 ± 0.031		
928.0	V	P	0.466 ± 0.029		
930.0	V	P	0.493 ± 0.031		
932.0	V	P	0.482 ± 0.030		
933.0	V	P	0.488 ± 0.032		
934.0	V	P	0.502 ± 0.033		
936.0	V	P	0.494 ± 0.035		
937.0	V	P	0.497 ± 0.052		
938.0	V	P	0.466 ± 0.033		
953.0	V	P	0.488 ± 0.030		
1181.0	V	P	0.531 ± 0.035		
1186.0	V	P	0.512 ± 0.050		
1202.0	V	P	0.488 ± 0.029		
1205.0	V	P	0.483 ± 0.031		
1218.0	V	P	0.493 ± 0.035		
1227.0	V	P	0.513 ± 0.031		
1243.0	V	P	0.525 ± 0.032		
1281.0	V	P	0.527 ± 0.032		
1282.0	V	P	0.537 ± 0.032		
1292.0	V	P	0.557 ± 0.033		
1307.0	V	P	0.557 ± 0.034		
1320.0	V	P	0.585 ± 0.037		
1337.0	V	P	0.566 ± 0.048		
2695.4	A ²	P	0.497 ± 0.028		
2695.4	A	S ^b	0.507 ± 0.029	0.97 ± 0.12	4.45 ± 0.18
2963.6	A	S	0.484 ± 0.028	0.96 ± 0.12	3.99 ± 0.16
2963.6	A	P	0.479 ± 0.027		
3047.3	A	P	0.473 ± 0.027		
3047.3	A	S	0.479 ± 0.027	0.96 ± 0.12	3.76 ± 0.15
3049.3	A	P	0.481 ± 0.027		
3049.3	A	S	0.484 ± 0.028	1.01 ± 0.13	4.29 ± 0.17
3388.4	A	P	0.495 ± 0.028		
3388.4	A	S	0.499 ± 0.028	1.02 ± 0.13	4.27 ± 0.17
3404.0	A	P	0.490 ± 0.028		
3474.0	A	P	0.491 ± 0.028		
3475.3	A	S	0.496 ± 0.028	1.00 ± 0.12	4.03 ± 0.16
3714.0	C ³	P	0.462 ± 0.015		
3745.0	C	P	0.470 ± 0.015		
3769.0	C	P	0.465 ± 0.015		
3772.0	A	P	0.476 ± 0.027		
3797.4	A	S	0.469 ± 0.027	0.90 ± 0.11	4.13 ± 0.17
3798.0	A	P	0.473 ± 0.027		
4050.0	C	P	0.474 ± 0.012		
4058.0	C	P	0.474 ± 0.015		
4066.0	C	P	0.476 ± 0.015		
4068.7	A	S	0.485 ± 0.028	0.94 ± 0.12	4.46 ± 0.18
4068.7	A	P	0.483 ± 0.028		
4085.0	C	P	0.471 ± 0.015		
4091.4	A	S	0.475 ± 0.027	0.93 ± 0.12	4.37 ± 0.18
4092.0	A	P	0.477 ± 0.027		
4127.0	C	P	0.474 ± 0.015		
4145.3	A	P	0.477 ± 0.027		
4145.3	A	S	0.473 ± 0.027	0.94 ± 0.12	3.85 ± 0.16
4201.3	A	P	0.474 ± 0.027		
4201.3	A	S	0.460 ± 0.026	0.88 ± 0.11	4.13 ± 0.17
4204.0	C	P	0.467 ± 0.015		

Table 2. Continued.

4238.0	C	P	0.499 ± 0.019		
4435.7	A	S	0.491 ± 0.028	0.97 ± 0.12	4.66 ± 0.19
4435.7	A	P	0.496 ± 0.028		
4472.5	A	P	0.483 ± 0.028		
4472.5	A	S	0.482 ± 0.027	0.92 ± 0.11	4.38 ± 0.18
4513.4	A	P	0.466 ± 0.027		
4513.4	A	S	0.469 ± 0.027	1.03 ± 0.13	4.03 ± 0.16
4747.0	C	P	0.479 ± 0.018		
4769.0	C	P	0.481 ± 0.015		
4806.0	C	P	0.499 ± 0.016		
4807.6	A	S	0.495 ± 0.028	0.97 ± 0.12	4.23 ± 0.17
4807.6	A	P	0.498 ± 0.028		
4835.4	A	S	0.497 ± 0.028	0.92 ± 0.11	4.66 ± 0.19
4836.0	A	P	0.486 ± 0.028		
4850.0	C	P	0.412 ± 0.029		
4852.0	C	P	0.461 ± 0.017		
4862.0	C	P	0.478 ± 0.015		
4884.3	A	P	0.488 ± 0.028		
4884.3	A	S	0.492 ± 0.028	0.95 ± 0.12	3.92 ± 0.16
4886.0	C	P	0.466 ± 0.017		
4892.0	C	P	0.468 ± 0.015		
4913.0	C	P	0.470 ± 0.015		
4914.4	A	P	0.485 ± 0.028		
4914.4	A	S	0.485 ± 0.028	1.04 ± 0.13	4.40 ± 0.18
4945.0	C	P	0.469 ± 0.015		
4979.0	C	P	0.455 ± 0.017		
5133.0	C	P	0.459 ± 0.015		
5155.0	C	P	0.454 ± 0.015		
5183.0	C	P	0.453 ± 0.014		
5247.0	C	P	0.437 ± 0.014		
5273.0	C	P	0.416 ± 0.013		
5298.0	C	P	0.421 ± 0.016		
5336.0	C	P	0.406 ± 0.013		
5511.0	C	P	0.378 ± 0.015		
5542.0	C	P	0.377 ± 0.017		
5565.0	C	P	0.375 ± 0.012		
5573.0	C	P	0.372 ± 0.013		
5591.0	C	P	0.374 ± 0.012		
5602.0	C	P	0.363 ± 0.012		
5618.0	C	P	0.361 ± 0.014		
5636.0	C	P	0.360 ± 0.013		
5653.3	A	P	0.345 ± 0.020		
5653.3	A	S	0.350 ± 0.020	1.35 ± 0.17	4.81 ± 0.19
5694.0	C	P	0.357 ± 0.013		
5894.5	A	P	0.374 ± 0.021		
5894.5	A	S	0.347 ± 0.020	1.34 ± 0.17	5.41 ± 0.22
5915.4	A	S	0.358 ± 0.020	1.28 ± 0.16	4.77 ± 0.19
5916.0	A	P	0.352 ± 0.020		
5923.0	C	P	0.361 ± 0.013		
5939.0	C	P	0.361 ± 0.012		
5945.0	C	P	0.350 ± 0.013		
5950.0	C	P	0.348 ± 0.020		
5956.0	C	P	0.349 ± 0.013		
5979.0	C	P	0.355 ± 0.013		
5984.0	C	P	0.352 ± 0.013		
5985.3	A	P	0.356 ± 0.020		
5985.3	A	S	0.347 ± 0.020	1.08 ± 0.14	5.10 ± 0.21
6008.0	C	P	0.357 ± 0.013		
6039.0	C	P	0.362 ± 0.014		
6238.4	A	S	0.377 ± 0.021	1.08 ± 0.14	4.52 ± 0.18

Table 2. Continued.

6238.4	A	P	0.386 ± 0.022		
6255.0	C	P	0.394 ± 0.013		
6272.0	C	P	0.392 ± 0.012		
6272.0	L ⁴	S	0.396 ± 0.023	1.18 ± 0.15	4.94 ± 0.20
6299.0	C	P	0.387 ± 0.012		
6307.0	C	P	0.392 ± 0.013		
6314.0	C	P	0.391 ± 0.012		
6325.0	C	P	0.395 ± 0.015		
6332.0	C	P	0.400 ± 0.013		
6338.0	C	P	0.396 ± 0.015		
6340.3	L	S	0.403 ± 0.023	1.36 ± 0.17	5.50 ± 0.22
6358.0	C	P	0.400 ± 0.013		
6374.0	C	P	0.401 ± 0.014		
6396.3	L	S	0.413 ± 0.024	1.27 ± 0.16	5.44 ± 0.22
6400.0	C	P	0.405 ± 0.013		
6421.4	L	S	0.425 ± 0.024	1.31 ± 0.16	5.20 ± 0.21
6429.0	C	P	0.408 ± 0.013		
6568.0	C	P	0.405 ± 0.013		
6588.0	C	P	0.410 ± 0.013		
6749.0	L	S	0.402 ± 0.023	1.02 ± 0.13	4.83 ± 0.20
6786.3	L	S	0.428 ± 0.024	1.01 ± 0.13	4.24 ± 0.17
7093.3	L	S	0.466 ± 0.027	1.13 ± 0.14	5.15 ± 0.21

¹0.5 m telescope at Climenhaga Observatory, University of Victoria (USA; Lewis et al. 1999)²1.82 m Copernico telescope at Asiago Observatory (Italy; Trevese et al. 2007)³Catalina Sky Survey (Drake et al. 2009)⁴1.52 m telescope at Loiano Observatory (Italy; Trevese et al. 2014)^aPhotometry^bSpectroscopy